Deformed Microcavity Quantum Cascade Lasers with Directional Emission

New Journal of Physics
The open-access journal for physics

Deformed microcavity quantum cascade lasers with directional emission

Qi Jie Wang[1], Changling Yan[1,2], Laurent Diehl[1,7], Martina Hentschel[3], Jan Wiersig[4], Nanfang Yu[1], Christian Pflügl[1], Mikhail A Belkin[1,5], Tadataka Edamura[6], Masamichi Yamanishi[6], Hirofumi Kan[6] and Federico Capasso[1,7]

[1] School of Engineering and Applied Sciences, Harvard University, Cambridge, MA 02138, USA

[2] Changchun University of Science and Technology, Changchun, 130022, People's Republic of China

[3] Max-Planck-Institut für Physik komplexer Systeme, Nöthnitzer Straße 38, D-01187 Dresden, Germany

[4] Institut für Theoretische Physik, Universität Magdeburg, Postfach 4120, D-39016 Magdeburg, Germany

[5] Now with Department of Electrical and Computer Engineering, University of Texas at Austin, TX 78758, USA

[6] Central Research Laboratory, Hamamatsu Photonics K.K., Hamamatsu 434-8601, Japan

E-mail: ldiehl@seas.harvard.edu and capasso@seas.harvard.edu

New Journal of Physics **11** (2009) 125018 (17pp)
Received 1 June 2009
Published 17 December 2009
Online at http://www.njp.org/
doi:10.1088/1367-2630/11/12/125018

Abstract. We report the experimental realization of deformed microcavity quantum cascade lasers (QCLs) with a Limaçon-shaped chaotic resonator. Directional light emission with a beam divergence of $\theta_{\parallel} \approx 33^{\circ}$ from QCLs emitting at $\lambda \approx 10\,\mu$m was obtained in the plane of the cavity for deformations in the range $0.37 < \varepsilon < 0.43$. An excellent agreement between measured and calculated far-field profiles was found. Both simulations and experiments show that the Limaçon-shaped microcavity preserves whispering gallery-like modes with high Q-factors for low deformations ($\varepsilon < 0.50$). In addition, while the measured spectra show a transition from whispering gallery-like modes to a more complex mode structure at higher pumping currents, we observed 'universal far-field behavior' for different intracavity mode distributions in the Limaçon

[7] Authors to whom any correspondence should be addressed.

microcavity, which can be explained by the distribution of unstable manifolds in ray optics simulations. Furthermore, the performance of the deformed microcavity lasers is robust with respect to variations of the deformation near its optimum value $\varepsilon = 0.40$, which implies that this structure reduces the requirements on photolithography fabrication. The successful realization of these microcavity lasers may lead to applications in optoelectronics.

Contents

1. Introduction

Microcavity lasers [1], which can confine light in a small mode volume with high quality-factor (Q-factor), have become an important subject of study [2]–[5] not only for optoelectronic applications with densely integrated optical components but also for fundamental studies such as cavity quantum electrodynamics, chaotic ray dynamics and nonlinear optical processes. In the past 20 years, significant progress has been made in designing whispering gallery mode (WGM) lasers [6, 7] such as micro-disks [8]–[10], micro-cylinder [11, 12], and micro-droplet lasers [13]. By employing total internal reflection, ultra-low threshold lasers [14, 15], and ultra-high Q-factor lasers [9, 16] have been demonstrated. Although microcavity lasers supporting WGMs have many advantages, a serious disadvantage is that their optical power output is low and their far-field profile is isotropic. Such properties limit their potential applications.

To improve the output coupling efficiency and directionality of microcavity lasers, various types of deformed structures [17]–[20] were proposed and/or demonstrated in a variety of gain media including polymers and semiconductors. These various geometries include quadrupolar-shaped lasers [21, 22], bow-tie lasers [23], asymmetric optical resonators with rational caustics [24, 25], stadium-shaped lasers [26], annular-shaped lasers [27] and spiral-shaped lasers [28]–[32].

Among these devices, electrically pumped mid-infrared quantum cascade lasers (QCLs) are of special interest [11], [22]–[24], [30, 31] because they are unipolar devices [33, 34], and hence they are not sensitive to undesirable surface recombination as is the case of diode lasers. In addition, mid-infrared QCLs have a relatively long emission wavelength, therefore reducing scattering losses due to roughness along the etched sidewalls of the microcavity. Finally their

TM polarization constrains the propagation to two dimensions, making it straightforward to relate the non-integrable ray dynamics of deformed resonators to shape changes. In summary microcavity QCLs are a model system to study situations when the optical wave equation is non-separable (as in deformed resonators), i.e. when the corresponding ray motion typically exhibits fully or partially chaotic dynamics, a limit known as quantum or wave chaos [23]. However, very few deformed QCLs have shown promise in terms of achieving highly directional emission, while preserving a relatively high Q [24], one of the key factors to achieve a reasonably low laser threshold. In addition, the Q-factor of these devices degrades significantly with increasing deformation due to the Q spoiling effect [35].

Recently, a novel Limaçon-shaped microcavity laser, capable of achieving directional light output while keeping high Q-factor whispering gallery-like modes, has been proposed [36] and demonstrated with QCLs [37]. In this paper, we report a comprehensive study of the mode spectra and beam profiles of mid-infrared QCLs with Limaçon-shaped microcavity. We have obtained whispering gallery-like mode QCLs emitting at $\lambda \approx 10\,\mu$m with a peak output power $\sim$10 mW and a far-field divergence angle $\theta_{\parallel} \approx 33^{\circ}$ in the plane to the cavity. A Q-factor of more than 1000, mostly limited by the high optical losses associated with free carrier absorption at mid-infrared wavelength, was deduced from the data. The far-field profiles of the Limaçon microcavity QCLs fabricated with various deformations were calculated based on both ray optics and wave simulations, and found to be in good agreement with experimental results. Compared with ridge QCLs, Limaçon-shaped microcavity QCLs have similar far-field divergence angles in both vertical and lateral directions with respect to the plane of the cavity, but lower threshold current densities. The successful demonstration of these microcavity lasers may lead to possible applications in photonic integrated circuits (PICs).

The paper is organized as follows: in section 2, the waveguide structure and the fabrication of the devices are discussed. In section 3, the performance of the Limaçon-shaped microcavity QCLs is reported, including light-current-voltage characteristics, mode spectra, lateral and vertical far-field profiles, threshold current densities, Q-factors and the robustness of the structure. Comprehensive numerical simulations are also presented in this section and compared with experimental results. Section 4 concludes the paper.

2. Device structure and fabrication

The deformed microcavity QCL was based on lattice matched $Ga_{0.47}In_{0.53}As/Al_{0.48}In_{0.52}As$ heterostructures grown by molecular beam epitaxy (MBE) on top of an n-doped (3×10^{18} cm^{-3}) InP substrate. The active region consists of 35 periodic stages, each consisting of a four-well double-phonon active region structure [38], targeted for light emission around 10 μm and a superlattice injector that also serves as an energy relaxation region for electrons exiting the previous stage. The active region is sandwiched between two 520 nm-thick n-doped (3×10^{16} cm^{-3}) InGaAs layers followed by two 3.5 μm-thick n-doped (1×10^{17} cm^{-3}) epitaxial InP cladding layers. A 0.5 μm-thick n-doped (5×10^{18} cm^{-3}) InP layer was deposited on the top of the cladding layer, followed by a 10 nm highly n-doped (1×10^{19} cm^{-3}) InP contact layer.

The QCL material was processed into a Limaçon-shaped structure, which is defined by $R(\theta) = R_0(1 + \varepsilon \cos\theta)$, where ε is the deformation factor and R_0 is the radius of curvature when $\theta = \pi/2$; see figure 1(a) for the optical microscope image of the top view of a device with $R_0 = 80\,\mu$m and $\varepsilon = 0.40$. We fabricated devices with different sizes $R_0 = 50$, 80 and 110 μm and different deformations $\varepsilon = 0.20$, 0.30, 0.37, 0.40, 0.43, 0.46, 0.50, 0.67, 0.70 and

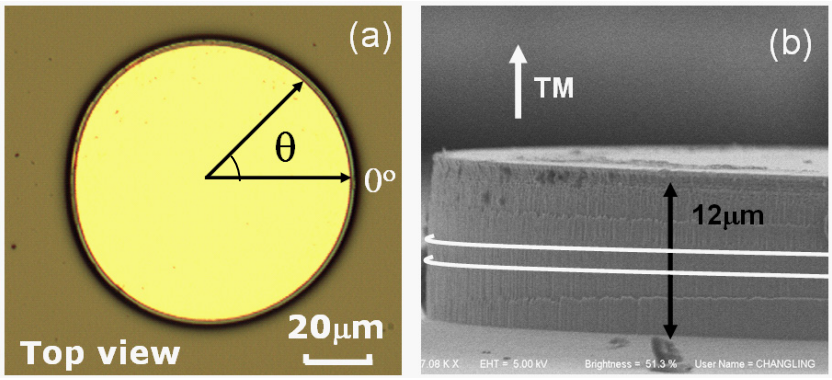

Figure 1. (a) Top view of the device with a deformation factor $\varepsilon = 0.4$ and $R_0 = 80\ \mu$m taken with an optical microscope. (b) Scanning electron microscope (SEM) image of the side view of the device showing a smooth sidewall, the two white lines indicate the position of the active region. The output of a QCL is intrinsically transverse magnetic (TM) polarized, as shown in the figure.

0.80. Photolithography was used to define the contour of the laser and the structure was etched through the gain medium using inductively coupled plasma reactive ion etching (ICP RIE). A recipe utilizing HCl, BCl_3 and Ar was optimized to obtain vertical and smooth sidewalls. Then, a top metal contact Ti/Au (10 nm/200 nm) was deposited by using electron-beam evaporation. The substrate was subsequently thinned down to about 200 μm, and a Ti/Au back contact was deposited. A scanning electron microscope (SEM) image of the device sidewall (figure 1(b)) shows a roughness of about 300 nm, which gives minor scattering considering that the wavelength of the laser is in the mid-infrared range. The devices were then soldered with indium to copper heat sinks and wire bonded. For each size and deformation of the structure, several samples were cleaved and tested to allow a repeatable and meaningful statistical analysis.

3. Device characterization and analysis

All of the devices tested, independent of their different sizes and deformations, demonstrated laser action at room temperature in pulsed mode operation at a duty cycle of 1% (pulse width 125 ns and repetition rate 80 kHz). We measured the electrical and power characteristics of the Limaçon-shaped QCLs, their optical mode spectra and the far-field profiles in the planes perpendicular and parallel to the cavity.

3.1. Light-current-voltage characteristics and comparison with ridge lasers

Figure 2(a) shows the light output power versus current (L–I) and voltage versus current (V–I), measured at 300 K, of a typical Limaçon-shaped laser with a deformation $\varepsilon = 0.4$ and a size $R_0 = 110\ \mu$m. The output power measurements were performed by using a calibrated thermopile detector and a polished metallic tube positioned along the direction given by $\theta = 0$ (see figure 1(a)) to collect the laser output. The inner diameter of the tube is 6 mm, corresponding to a collection angle of the laser output of about 100°. This detection geometry

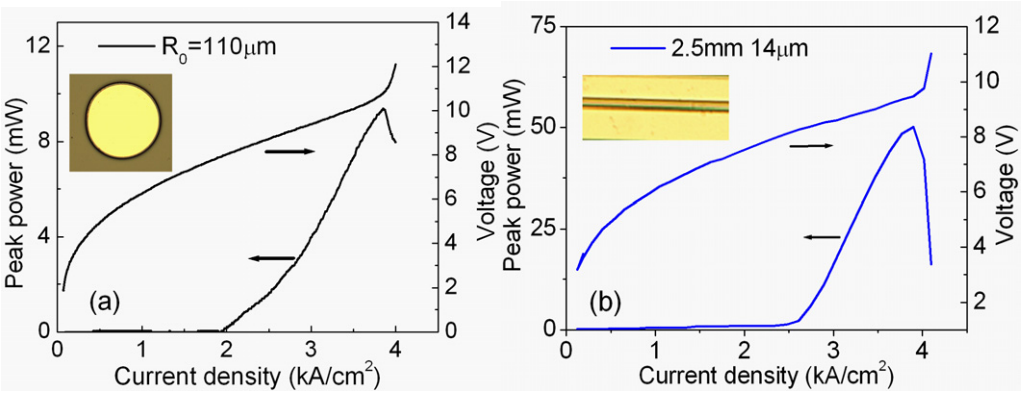

Figure 2. Room temperature light–current–voltage (L–I–V) characteristics of Limaçon microcavity QC lasers and ridge waveguide QC lasers with similar sizes measured in pulsed mode operation with a duty cycle of 1%. (a) L–I–V characteristics of a Limaçon laser with $R_0 = 110\,\mu$m and $\varepsilon = 0.40$. (b) L–I–V characteristics of a ridge waveguide laser with ridge length of 2.5 mm and a width of 14 μm from one facet without high reflection coating.

was used in order to collect the light concentrated in the main lobe present in the far-field, which contains more than 50% of the total output power emitted in all directions as illustrated in section 3.3.

As shown in figure 2(a), a peak output power from the main peak close to 10 mW was obtained. The threshold current density of this Limaçon microcavity laser is about 2.0 kA cm^{-2}. To compare this light output level with that of a traditional edge-emitting ridge QC lasers with similar sizes, we fabricated ridge QC lasers from the same wafer material and measured the voltage–current and output power–current characteristics from a device with a length of 2.5 mm and 14 μm width. The results are shown in figure 2(b). The maximum peak power from one facet of the ridge laser was close to 50 mW, and the threshold current density is about 2.6 kA cm^{-2}. Due to the presence of whispering gallery-like modes with high Q-factors (as discussed below), the Limaçon microcavity has a lower threshold current density. However, because only a small fraction (along the boundary of the cavity due to the presence of whispering gallery-like modes) of the pumped volume participates in the generation of photons, the output power is lower than that of the ridge laser.

The light output power characteristics as a function of the deformations from various Limaçon-shaped lasers with the same size $R_0 = 80\,\mu$m were also measured, as shown in figure 3 (square symbols). The collected output power increases with increasing deformation ε because more optical power is coupled out of the cavity. The dependence of the far-field and the outcoupling as a function of deformation is discussed in the section 3.3. The maximum output power integrated over all directions is also shown in figure 3 and was determined by multiplying: (i) the maximum power obtained with the powermeter aligned along the $\theta = 0^{\circ}$ direction and (ii) the ratio of intensity emitted by the devices over 360° and between $\theta = \pm 50^{\circ}$ (corresponding to the collection angle of our power meter). This ratio was deduced by integrating the measured far-field data.

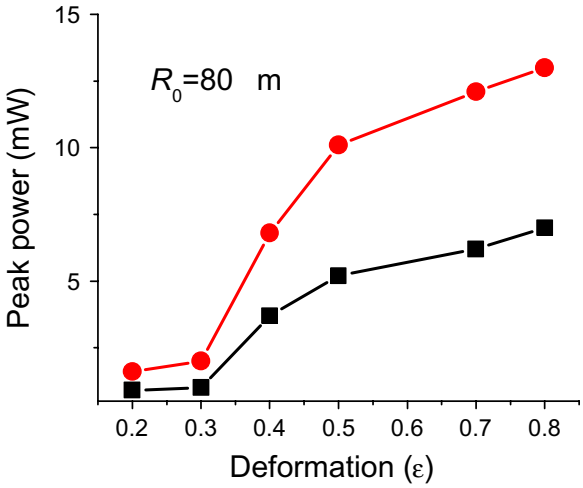

Figure 3. Maximum optical power as a function of deformation from various devices with the same $R_0 = 80\,\mu$m. The output power was collected along the $\theta = 0$ direction (square symbols). The data corresponding to the power integrated over all directions is represented by circles in the graph. The lines connecting the symbols are a guide to the eye.

3.2. Spectral characterization

The emission spectrum of a number of devices was characterized using a high-resolution Fourier transform infrared spectrometer (FTIR) equipped with a liquid nitrogen cooled mercury–cadmium–telluride (MCT) detector. Figure 4(a) shows the emission spectra (resolution of $0.125\,\text{cm}^{-1}$) of a Limaçon microcavity QCL with $R_0 = 80\,\mu$m and deformation $\varepsilon = 0.40$ measured at different pumping levels along the $\theta = 0$ direction. We note that the spectra measured at any angle were identical to the ones measured under the conditions described above. As shown in figure 4(a), the laser emission is single mode with an emission wavelength of $\lambda \approx 9.8\,\mu$m (wavenumber $1/\lambda = 1018\,\text{cm}^{-1}$) close to threshold current (380 mA). At a pumping current of 500 mA, two sets of optical modes appear, corresponding to the two highest Q-factor whispering gallery-like modes (see figures 7(a) and (b)). One set of modes has features at 996.87, 1003.16 and $1009.17\,\text{cm}^{-1}$ while the other set has peaks positioned at 1012.11, 1018.05 and $1023.87\,\text{cm}^{-1}$. The mode spacing in each set is approximately $6.0\,\text{cm}^{-1}$. This value agrees very well with the calculated mode spacing ($6.2\,\text{cm}^{-1}$) for fundamental WGMs given by $1/(L^* n_{\text{eff}})$, where L is the perimeter of the structure, and $n_{\text{eff}} \approx 3.2$ is the effective refractive index for TM polarization, deduced from the mode spacing of a Fabry–Perot type ridge laser. Note that the polarization of QCLs is TM due to the selection rules of intersubbard transitions. At currents close to the roll-over of the L–I curve, additional non-WGMs appear at 1007.17, 1010.40, 1010.89 and $1014.92\,\text{cm}^{-1}$.

It is intuitively understandable that if $\varepsilon \geqslant 0.50$, the Limaçon microcavity cannot support whispering gallery-like modes because the shape of the boundary changes significantly from a circle (as shown in the insets of figure 6). To verify this, we measured the emission spectra of Limaçon microcavity QC lasers with higher deformations. Figure 4(b) shows the results obtained with a device characterized by $R_0 = 110\,\mu$m and $\varepsilon = 0.70$ measured at different pumping levels along the $\theta = 0$ direction. There is no sign of equally spaced modes in the

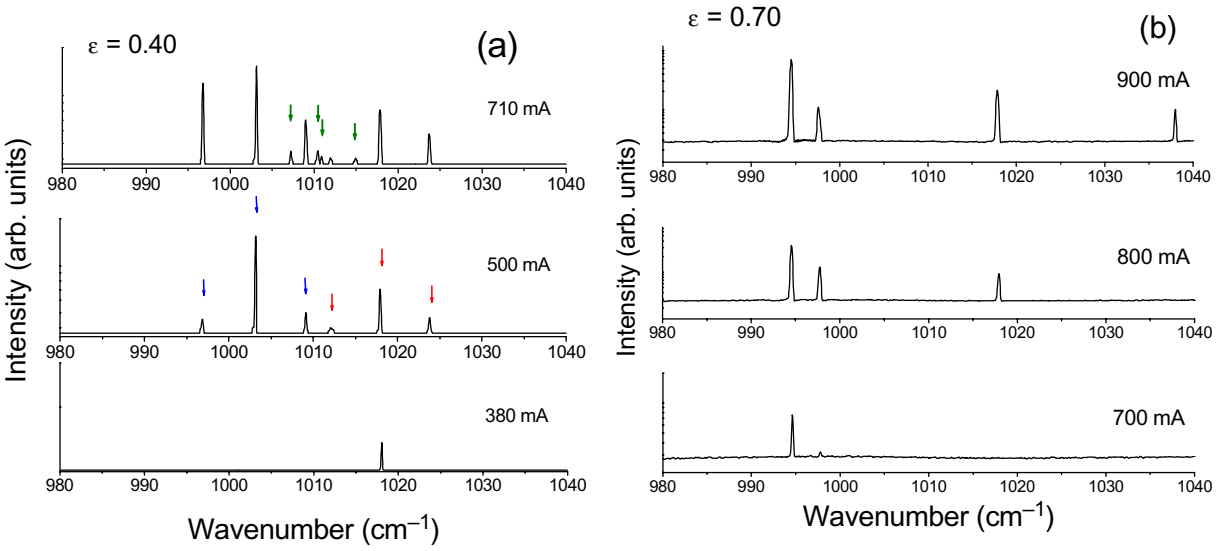

Figure 4. (a) Laser spectra of the Limaçon microcavity QC laser with $R_0 = 80\,\mu$m and $\varepsilon = 0.40$ at different pumping currents. The threshold current of the laser is around 380 mA. At a pumping current of 500 mA, two sets of whispering gallery-like modes, indicated by the blue and red arrows are shown; at an even higher pumping current (710 mA), several additional non-WGMs appear, shown by the green arrows. (b) Laser emission spectra of the Limaçon microcavity QC laser with $R_0 = 110\,\mu$m deformation $\varepsilon = 0.70$ at different pumping currents. At these pumping currents, no sign of whispering gallery-like modes with mode spacing $1/(L^* n_{\text{eff}})$ corresponding to the device perimeter L was seen in the spectra.

spectra corresponding to WGMs with mode spacing $1/(L^* n_{\text{eff}})$. In section 3.3.1, we will discuss in detail the transition from whispering gallery-like modes to non-WGMs when the deformation factor increases.

3.3. Far-field profile

3.3.1. Ray optics and wave simulations. The far-field profiles in the plane perpendicular to the QCL growth direction were first calculated with ray optics simulations. The simulations were carried out by starting a set of 30 000 rays along the cavity boundary (arc length s measured from the $\theta = 0$ direction, angle of incidence χ at the cavity boundary) with whispering gallery-like mode initial conditions ($0.8 < |\sin\chi| < 1$). The rays propagate following the laws of specular reflection, using Fresnel laws (see [36] for details). Light escaping the cavity according to Snell's law was collected as the far-field characteristics. Note that since the radius of curvature at any point along the resonator boundary is much larger than the wavelength in the material the use of Fresnel and Snell laws is valid. Figure 5(a) shows the Poincaré surface of section (SOS) of rays leaving the Limaçon cavity with deformation $\varepsilon = 0.4$ and $R_0 = 80\,\mu$m. The character of the ray trajectories is chaotic, while the far-field profile is determined by the path in phase space that the rays take to escape the cavity by entering the leaky region, defined by the critical lines, $-1/n_{\text{eff}} < \sin\chi < 1/n_{\text{eff}}$ (the sign of χ distinguishes the two possible senses of rotation), where the condition of total internal reflection is no longer fulfilled (the entity of these points is the

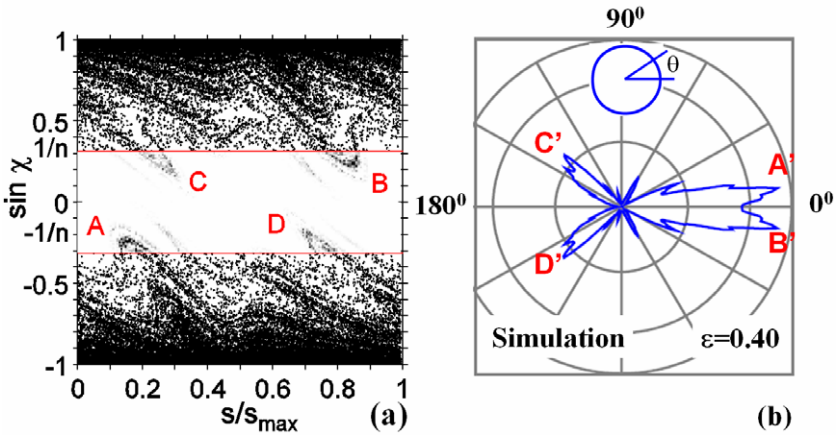

Figure 5. (a) Poincaré SOS of rays leaving the Limaçon cavity with deformation $\varepsilon = 0.40$ and $R_0 = 80\,\mu$m. For each reflection at the cavity boundary, the arc length s (with $s_{\max}$ being the cavity perimeter) and the sine of the angle of incidence χ are shown. Between the critical lines, shown in red, the ray intensity is weighted by the Fresnel coefficients (for TM polarization). The resulting accumulated intensity is shown in gray scale and represents the so-called unstable manifold. It determines the far-field pattern of the cavity that is shown in (b) in the polar coordinate system. The main far-field peaks are labeled as A′, B′, C′ and D′ corresponding to the escape regions A, B, C and D, respectively, as marked in (a).

so-called unstable manifold). The resulting far-field profile possesses a pronounced emission lobe around the 0 line direction for $\varepsilon = 0.40$ as shown in figure 5(b). The main emission lobes A′, B′, C′ and D′ in figure 5(b) can be related to the escape regions A, B, C and D, respectively, shown in figure 5(a). The escape paths from A, B, C and D are also discussed in wave simulations in the later part of this section. The comprehensive far-field profiles with various deformations from 0.2 to 0.7 were also calculated as shown in figure 6.

From the simulations, we observed that the optimum deformation is around $\varepsilon = 0.40$, as it gives the smallest far-field divergence, defined as the full-width at half-maximum (FWHM) of the main far-field lobe along the $\theta = 0$ line. The divergence of the optimal structure is about 30°. We notice that for $\varepsilon = 0.20$, the far-field divergence angle is comparable to that of $\varepsilon = 0.40$; however, the output power is dramatically smaller than that of $\varepsilon = 0.40$, by a factor of more than 10 times according to both simulations and experiments (see figure 3). This is because $\varepsilon = 0.20$ corresponds to a geometry very close to a circular disk and hence the output power is small.

We also carried out wave simulations on the Limaçon structures by solving Maxwell equations numerically using the finite element method; detailed information on our simulation technique can be found in [39]. Figures 7(a)–(c) show the intensity distribution of some TM modes calculated for a structure with $\varepsilon = 0.40$ and $R_0 = 80\,\mu$m. The insets show the corresponding external near-field patterns. The modes in figures 7(a) and (b) are the two highest Q whispering gallery-like modes with (theoretical) Q-factors $> 10^7$, and thus can be excited at a low pumping current above threshold. It is therefore reasonable to assume that they correspond to the two sets of whispering gallery-like mode observed in the experiment as shown in figure 4(a) at a pumping current of 500 mA. The mode in figure 7(c) has a medium

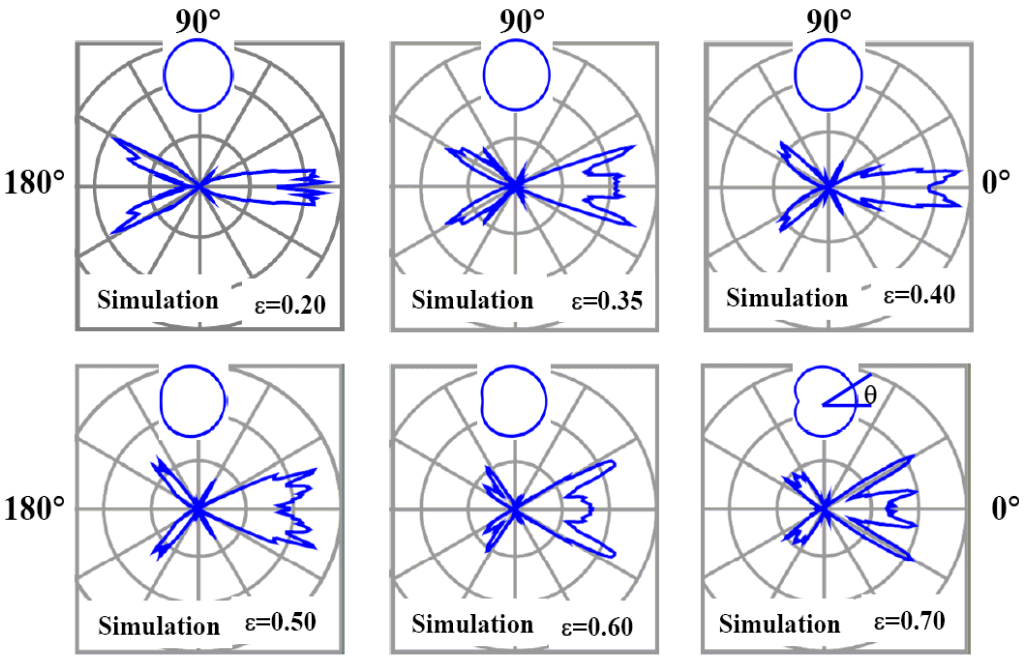

Figure 6. Calculated far-field profiles of the microcavity QCLs with different deformations $\varepsilon = 0.20$, 0.35, 0.40, 0.50, 0.60 and 0.70, by using ray optics simulations (radius $R_0 = 80\,\mu$m). Insets are sketches of the corresponding device cavities. The relative power levels for different ε are not reflected in these figures.

Q-factor of about 18 000 and is similar to the modes observed in [36]. Interestingly, all these three modes (and in fact all medium-Q and high-Q modes that we studied) show similar external near-field patterns (see the insets of figures 7(a)–(c)) and far-field patterns (see the inset of figure 7(d)). This is what is called 'universal far-field behavior', which was also studied and observed previously in other deformed microcavities [40]. The reason for this 'universal far-field behavior' is that the emission directionality is mainly determined by the structure of the unstable manifolds in the leaky region, as seen in figure 5(a), which are determined by the geometric shape of the deformed microcavity, regardless of the different spatial distributions of these modes inside the cavity. Furthermore, the wave simulation agrees very well with the ray optics simulation, as shown in figure 7(d). The results of these two simulation techniques differ just in some minor details which prove the validity of the two methods.

To illustrate the transition from whispering gallery-like modes to non-WGMs when increasing the deformations of Limaçon microcavity QC lasers, as discussed experimentally in figures 4(a) and (b), we performed wave simulations with different deformations $\varepsilon = 0.5$ and 0.6 while keeping $R_0 = 80\,\mu$m. As shown in figure 8(a), a transition from whispering gallery-like modes to a more complex structure (we refer this to the quasi-WG-type mode) occurs for $\varepsilon = 0.5$. While at $\varepsilon = 0.6$, see figure 8(b), the highest Q-factor mode is not whispering gallery-like but a quite complex distribution in the cavity. Therefore, combining the simulations of figures 7(a) and (b) with those of figures 8(a) and (b), we can expect whispering gallery-like modes for $\varepsilon < 0.5$, quasi-WG-type mode at $\varepsilon = 0.5$, and non-WGMs for $\varepsilon > 0.5$ in the Limaçon microcavities.

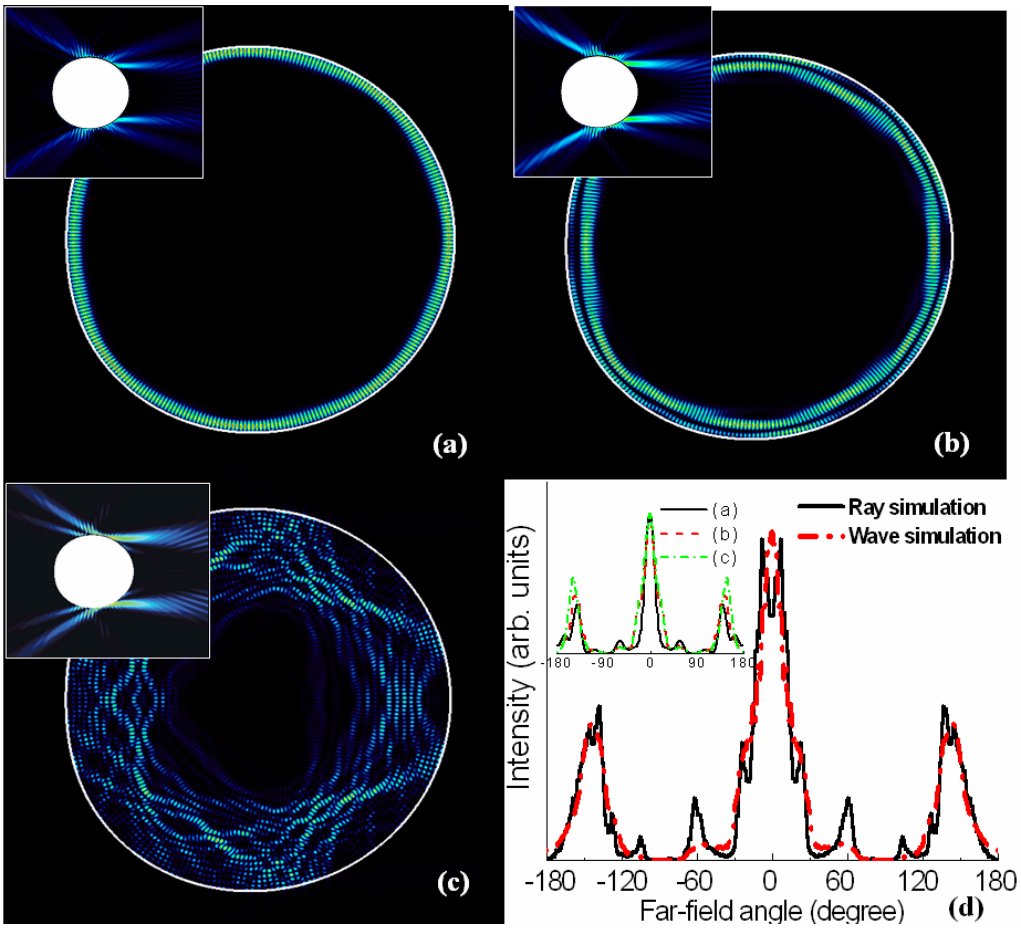

Figure 7. Intensity distribution of the TM modes inside the cavity calculated with wave simulations ($\varepsilon = 0.40$ and $R_0 = 80\,\mu$m): (a) the highest quality-factor (Q-factor) whispering gallery-like mode; (b) the second highest Q-factor whispering gallery-like mode; (c) one of the low Q-factor modes, and each inset of (a–c) is the external intensity distribution of the corresponding mode; (d) comparison of the far-field profiles obtained with wave simulation (corresponding to the mode in (a)) and ray optics simulation, the inset shows that the far-field profiles of the three different modes in (a–c) are similar. All far-field profiles are normalized to their maximum values. Note the modes have very similar far-field profiles, the so-called 'universal far-field behavior'.

3.3.2. Far-field measurements. To measure the far-field profiles, we used a setup based on a motorized rotation stage [41]: the laser was placed on a sample holder fixed at the center of the rotation stage. An MCT detector positioned on an arm attached to the stage was scanned in the far field. The setup has an angular resolution of about 0.25° and the samples were rotated in steps of 0.5°. The measurement of far-field profiles was performed over 360°.

We obtained a very good overall agreement between the simulated and measured far-field profiles. Shown in figure 9 are the experimental (solid line) and simulation (dotted line) results for a device with $\varepsilon = 0.40$ and $R_0 = 80\,\mu$m at a pumping current of 500 mA. Directional emission was obtained in the far-field with an angular divergence (FWHM) of around 33° for

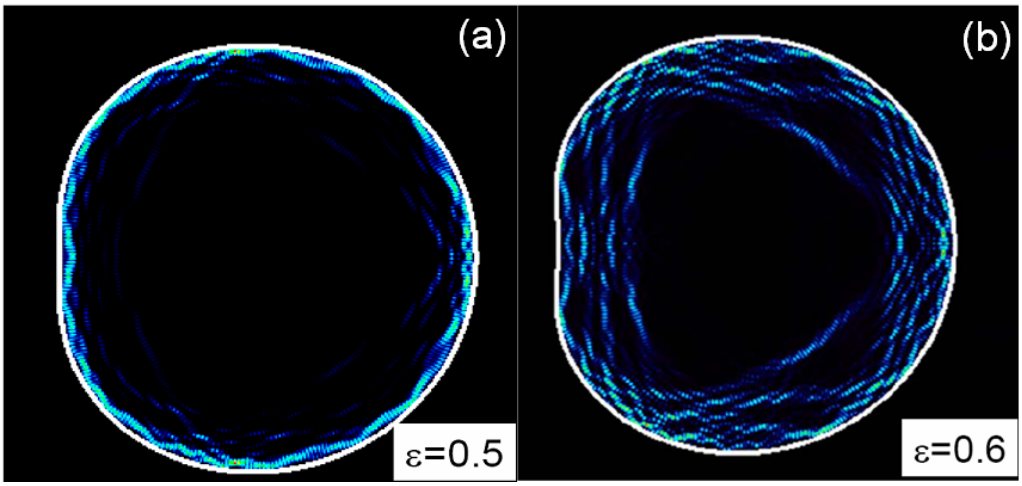

Figure 8. Intensity distributions of the highest Q-factor TM modes inside the laser cavity calculated with wave simulation for $R_0 = 80\,\mu$m and deformations (a) $\varepsilon = 0.50$ with quasi-WG-type mode and (b) $\varepsilon = 0.60$ with non-WGMs.

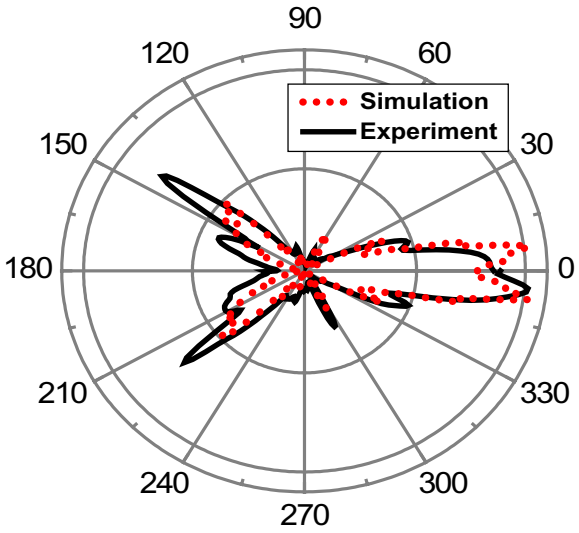

Figure 9. Ray optics simulation (dotted line) and experimental (solid line) lateral far-field profiles in polar coordinate for a device with $\varepsilon = 0.40$ and $R_0 = 80\,\mu$m at a pumping current of 500 mA. The far-field profiles are normalized to their maximum values.

this device, which is smaller than those reported for stadium-shaped lasers [42], QC spiral lasers [29] and rational caustic resonator laser [24] ($\sim$35°). The most intense feature in the far field appears in the $\theta = 0$ direction, and is approximately twice as large in terms of power level compared to the two side peaks near the $\theta = \pm 135°$ directions. The small discrepancy of the FWHM of the main peak between the experimental result (33°) and the ray optics simulation (30°) is most likely due to the surface roughness that broadens the main lobe. For other measured devices with $R_0 = 50$ and $110\,\mu$m and $\varepsilon = 0.40$, similar directional emission was also obtained

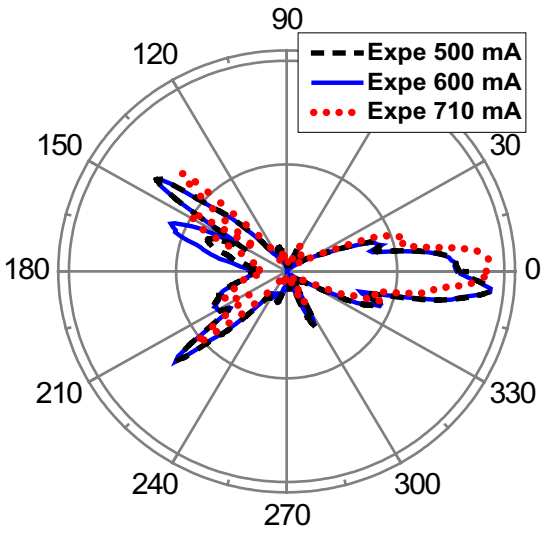

Figure 10. Measured far-field profiles from a Limaçon cavity QCL with the optimized deformation factor $\varepsilon = 0.40$ under different pumping currents of (a) 500 mA, (b) 600 mA and (c) 710 mA, respectively. The threshold current of this device is about 380 mA. The far-field profiles are normalized to their maximum values.

demonstrating that the far-field profile of the Limaçon structure is independent of the size once R_0 is reasonably larger than the emission wavelength in the cavity.

The far-field profiles were essentially independent of the pumping current. Figure 10 shows the evolution of the far-field profiles as a function of pumping current for a representative device with $R_0 = 80\,\mu$m and $\varepsilon = 0.40$. At higher pumping current, lower Q-factor non-WGMs appear (figure 4(a)); however because of the property of 'universal far-field behavior' the far-field profile of this device is not significantly changed as the pumping current increases from 500 to 600 mA and 710 mA.

We also measured the far-field pattern of the Limaçon-shaped lasers in the direction parallel to the growth direction. As expected, the vertical far-field profile exhibits a similar divergence angle about 80°comparable to that of the ridge laser device [41].

3.3.3. Sensitivity of far-field profiles to deformation. For a low deformation factor of $\varepsilon = 0.20$, our simulations show a directional emission along the $\theta = 0$ direction as seen in figure 11(a) (the dotted line). Experimentally, we obtained however a broader main lobe with multiple peaks (the solid line). This is mainly due to the fact that the output power of a microcavity with a small cavity deformation is too weak to dominate over the parasitic scattering due to the inevitable surface roughness. We also noticed that when ε is small the peak positions in the far-field for different devices are actually different, thus supporting the notion that for small deformation, the effects of roughness scattering dominates the features present in the far-field. At a higher deformation factor of $\varepsilon = 0.67$ the experimental (solid line) and simulation (dash line) far-field profiles show a main lobe containing several sub-peaks with larger divergence angles around 60°; see figure 11(b). There is a very good agreement between the simulation and experimental results.

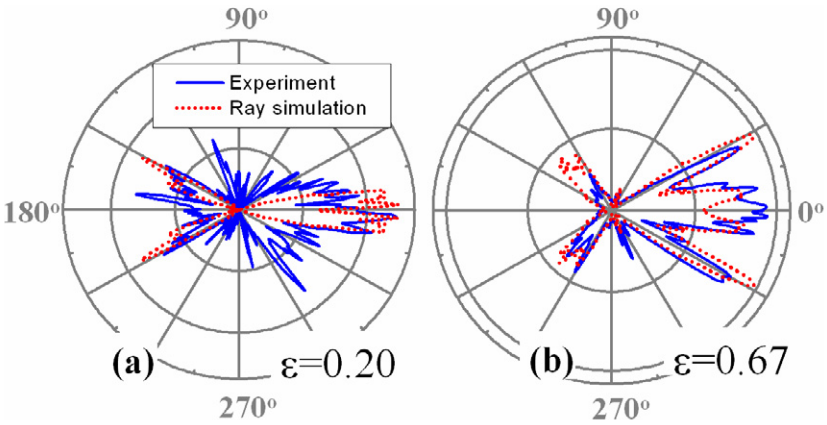

Figure 11. Comparison between the ray simulation and experimental far-field patterns for Limaçon cavity QCLs with different deformation factors: (a) the experimental (solid line) and simulation (dash line) results with $\varepsilon = 0.20$ and (b) the experimental (solid line) and simulation (dash line) results with $\varepsilon = 0.67$.

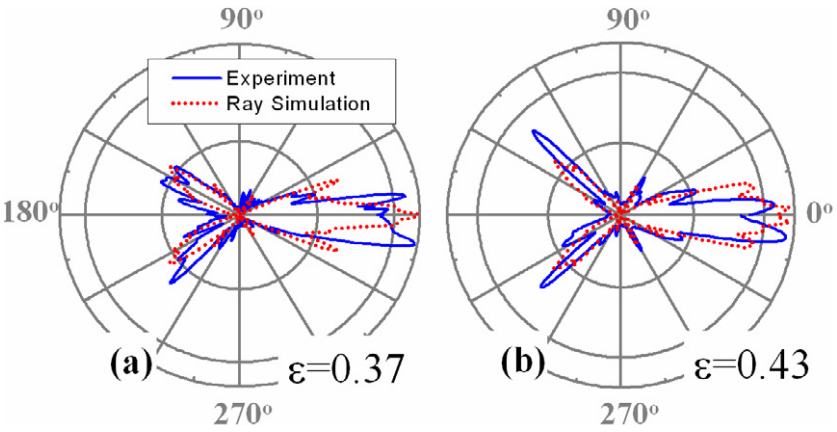

Figure 12. Comparison between the experimental and the simulation far-field profiles for Limaçon cavity QCLs with different deformations: (a) the experimental (solid line) and simulation (dotted line) results with $\varepsilon = 0.37$ and (b) the experimental (solid line) and simulation (dotted line) results with $\varepsilon = 0.43$.

To further investigate the dependence of the far-field profile on the deformation factor ε, we processed several samples with $\varepsilon = 0.37$ and 0.43, and measured their far-field profile. In this range of cavity deformation, the maximum difference in the cavity sizes along the short axis for $R_0 = 80\,\mu$m devices about 5 μm, well within the fabrication resolution of photolithography. Figure 12 demonstrates that the experimental (solid line) and the simulation (dotted line) results show reasonably good agreement. The shape, the position and FWHM of the main lobe of the far-field profiles are insensitive to the deformations of Limaçon structure from $\varepsilon = 0.37$ to 0.43.

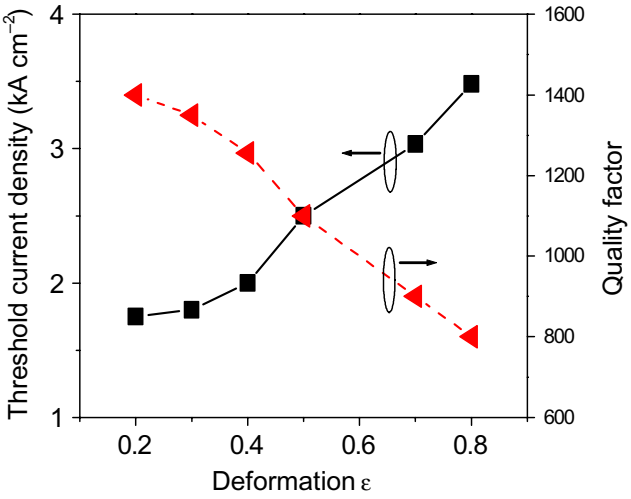

Figure 13. Threshold current density and the corresponding quality factor of the Limaçon cavity, calculated from the data, as a function of deformation factor. The size of the structure is fixed at $R_0 = 80\,\mu$m.

3.4. Threshold current density and quality factor

We also characterized the threshold current density and the quality factor of the Limaçon microcavity. The Q factor can be expressed as $Q = 2\pi n_{\text{eff}}/(\lambda_0 J_{\text{th}} g \Gamma_{\text{act}})$, where λ_0 is the wavelength in vacuum, J_{th} is the threshold current density, g is the gain coefficient, and Γ_{act} is the mode confinement factor for the active region [4]. The gain coefficient and the waveguide losses α_{w} of the microcavity laser can be estimated from the measurement of ridge waveguide lasers by studying the dependence of the threshold current density on the cavity length. From ridge laser devices processed from the same material with different lengths, we deduced $g\Gamma_{\text{act}} = 8.0 \times 10^{-3}\,\text{cm A}^{-1}$, and $\alpha_{\text{w}} = 15.6\,\text{cm}^{-1}$ using the relationship $J_{\text{th,ridge}} = (\alpha_{\text{m}} + \alpha_{\text{w}})/g\Gamma_{\text{act}}$ [34]. Since the waveguide losses of the microcavity laser are nearly the same to those of the Fabry–Perot ridge laser while the threshold current density is smaller, the value of the scattering losses including the out-coupling loss is small ($\alpha_{\text{out}} = 0.4\,\text{cm}^{-1}$) as deduced from $J_{\text{th}} = (\alpha_{\text{out}} + \alpha_{\text{w}})/g\Gamma_{\text{act}}$ (for microcavity laser). This demonstrates that the losses in the Limaçon microcavity are mainly dominated by the waveguide losses. For $\varepsilon = 0.40$ a Q-factor around 1250 is obtained. It is larger than that of the other deformed microcavity lasers emitting at a similar wavelength at low temperature [4]. This Q factor is even similar to that of the circular-shaped QCLs [22], and it is also comparable to those that were calculated for circular semiconductor microcavities [43]. This is not surprising due to material and device processing improvements since those earlier reports and to the Limaçon resonator, which supports high Q-factor whispering gallery-like modes. We note that, due to the high optical losses associated with free carrier absorption at mid-infrared wavelengths, the measured Q-factor in our devices is much smaller than the value obtained in simulations, where the free-carrier waveguide losses are not considered. The quality factor and threshold current density as a function of the deformation parameter ε of the Limaçon structure is shown in figure 13. As expected, the larger the deformation, the lower the quality factor and the higher the threshold current density. A structure with a lower deformation gives a more confined whispering gallery-like mode,

Table 1. Characteristics of the Limaçon structure with respect to different deformations near the optimum $\varepsilon = 0.40$ with $R_0 = 80\,\mu$m.

ε	Threshold current density (kA cm^{-2})	Q-factor	Optical power (mW)	Slope efficiency (mW A^{-1})
0.37	1.96	1282	3.4	11
0.40	2.00	1256	4.0	12
0.43	2.09	1203	4.6	15

which results in a lower coupling loss, and therefore a lower threshold current density and a lower output power.

3.5. Robustness of the Limaçon QCLs performance with respect to variations of the deformation

We also conducted a systematic experimental study on the robustness of the Limaçon QCL performance with respect to the variation of the deformation factor. The threshold current density, light power, slope efficiency and Q-factor of different samples with different deformations $\varepsilon = 0.37$, 0.40 and 0.43 are shown in table 1. The threshold currents and Q-factor values are remarkably insensitive to variations in ε in that range, while the output power and thus the slope efficiency improve slightly with increasing the deformation. These results, together with the fact that the far-field profile of Limaçon lasers does not vary significantly for ε comprised between 0.37 and 0.43 (see section 3.3.4) show the robustness of the characteristics of Limaçon microcavity structure with respect to deformations near the optimum value. This property significantly reduces the requirements on precise photolithography fabrication of the structure.

4. Conclusion

Limaçon-shaped microcavity QCLs operating at room temperature have been systematically studied and experimentally demonstrated at $\lambda \approx 10\,\mu$m. Low divergence light emission and whispering gallery-like modes were observed from the Limaçon-shaped microcavity with deformations $0.37 < \varepsilon < 0.4$. The measured far-field profiles are in excellent agreement with the results of both ray optics and wave simulations. Peak optical power of about 10 mW at room temperature was obtained from a 110 μm-radius device. In addition, the unique robustness of the performance of the Limaçon microcavity structure against the variation of the deformation near its optimal value was demonstrated experimentally.

Acknowledgments

This work was supported by the AFOSR (FA9550-08-1-0047). Financial support from the DFG research group 760 is gratefully acknowledged by Jan Wiersig and Martina Hentschel who in addition acknowledges support within the DFG Emmy-Noether Programme. The structures were processed in the Center for Nanoscale Science (CNS) in Harvard University. Harvard–CNS

is a member of the National Nanotechnology Infrastructure Network. CY acknowledges support from the China Scholarship Council (CSC) visiting scholarship.

References

[1] Vahala K J 2003 Optical microcavities *Nature* **424** 839–46
[2] Qian S-X, Snow J B, Tzeng H-M and Chang R K 1986 Lasing droplets: highlighting the liquid-air interface by laser emission *Science* **231** 486–8
[3] Levi A F J, Slusher R E, McCall S L, Pearton S J and Hobson W S 1993 Room-temperature lasing action in $In_{0.51}Ga_{0.49}P/In_{0.2}Ga_{0.8}As$ microcylinder laser diodes *Appl. Phys. Lett.* **62** 2021–3
[4] Gmachl C, Faist J, Capasso F, Sirtori C, Sivco D L and Cho A Y 1997 Long-wavelength (9.5–11.5 μm) microdisk quantum cascade lasers *IEEE J. Quantum Electron.* **33** 1567–73
[5] Fujita M, Sakai A and Baba T 1999 Ultrasmall and ultralow threshold GaInAsP-InP microdisk injection lasers: design, fabrication, lasing characteristics, and spontaneous emission factor *IEEE J. Sel. Top. Quantum Electron.* **5** 673–81
[6] Matsko A B and Ilchenko V S 2006 Optical resonators with whispersing-gallery modes – part I: basics *IEEE J. Sel. Top. Quantum Electron.* **12** 3–14
[7] Ilchenko V S and Matsko A B 2006 Optical resonators with whispering-gallery modes – part II: applications *IEEE J. Sel. Top. Quantum Electron.* **12** 15–32
[8] McCall S L, Levi A F J, Slusher R E, Pearton S J and Logan R A 1992 Whispering-gallery mode microdisk lasers *Appl. Phys. Lett.* **60** 289–91
[9] Kippenberg T J, Kalkman J, Ploman A and Vahala K J 2006 Demonstration of an erbium-doped microdisk laser on a silicon chip *Phys. Rev.* A **74** 051802
[10] Song Q, Cao H, Ho S T and Solomon G S 2009 Near-IR subwavelength microdisk lasers *Appl. Phys. Lett.* **94** 061109
[11] Gianordoli S, Hvozdara L, Strasser G, Schrenk W, Unterrainer K and Gornik E 1999 GaAs/AlGaAs-based microcylinder lasers emitting at 10 μm *Appl. Phys. Lett.* **75** 1045–7
[12] Anders S, Schrenk W, Gornik E and Strasser G 2002 Room-temperature operation of electrically pumped quantum-cascade microcylinder lasers *Appl. Phys. Lett.* **80** 4094–6
[13] Saito M, Shimatani H and Naruhashi H 2008 Tunable whispering gallery mode emission from a microdroplet in elastomer *Opt. Express* **16** 11915–9
[14] Park H-G, Kim S-H, Kwon S-H, Ju Y-G, Yang J-K, Baek J-H, Kim S-B and Lee Y-H 2004 Electrically driven single-cell photonic crystal laser *Science* **305** 1444–7
[15] Ulrich S M, Gies C, Ates S, Wiersig J, Reitzenstein S, Hofmann C, Lőffler A, Forchel A, Jahnke F and Michler P 2007 Photon statistics of semiconductor microcavity lasers *Phys. Rev. Lett.* **98** 043906
[16] Michael C P, Srinivasan K, Johnson T J, Painter O, Lee K H, Hennessy K, Kim H and Hu E 2007 Wavelength- and material-dependent absorption in GaAs and AlGaAs microcavities *Appl. Phys. Lett.* **90** 051108
[17] Levi A F J, Slusher R E, McCall S L, Glass J L, Pearton S J and Logan R A 1993 Directional light coupling from microdisk lasers *Appl. Phys. Lett.* **62** 561–3
[18] Nockel J U, Stone A D, Chen G, Grossman H L and Chang R K 1996 Directional emission from asymmetric resonant cavities *Opt. Lett.* **21** 1609–11
[19] Chang R K and Campillo A J (ed) 1996 *Optical Processes in Microcavities* (New York: World Scientific)
[20] Lee S B, Lee J H, Chang J S, Moon H J, Kim S W and An K 2002 Observation of scarred modes in asymmetrically deformed microcylinder lasers *Phys. Rev. Lett.* **88** 033903
[21] Nockel J U and Stone A D 1997 Ray and wave chaos in asymmetric resonant optical cavities *Nature* **385** 45–7
[22] Gianordoli S, Hvozdara L, Strasser G, Schrenk W, Faist J and Gornik E 2000 Long-wavelength ($\lambda = 10\,\mu$m) quadrupolar-shaped GaAs-AlGaAs microlasers *IEEE J. Quantum Electron.* **36** 458–64

[23] Gmachl C, Capasso F, Narimanov E E, Nockel J U, Stone A D, Faist J, Sivco D L and Cho A Y 1998 High-power directional emission from microlasers with chaotic resonators *Science* **280** 1556–64
[24] Baryshnikov Y, Heider P, Parz W and Zharnitsky V 2004 Whispering gallery modes inside asymmetric resonant cavities *Phys. Rev. Lett.* **93** 133902
[25] Gao J, Heider P, Chen C J, Yang X, Husko C A and Wong C W 2007 Observation of interior whispering gallery modes in asymmetric optical resonators with rational caustics *Appl. Phys. Lett.* **91** 181101
[26] Fang W, Cao H and Solomon G S 2007 Control of lasing in fully chaotic open microcavities by tailoring the shape factor *Appl. Phys. Lett.* **90** 081108
[27] Wiersig J and Hentschel M 2006 Unidirectional light emission from high-Q modes in optical microcavities *Phys. Rev.* A **73** 031802
[28] Chern G D, Tureci H E, Stone A D, Chang R K, Kneissl M and Johnson N M 2003 *Appl. Phys. Lett.* **83** 1710–2
[29] Kneissl M, Teepe M, Miyashita N, Johnson N M, Chern G D and Chang R K 2004 Current-injection spiral-shaped microcavity disk laser diodes with unidirectional emission *Appl. Phys. Lett.* **84** 2485–7
[30] Audet R *et al* 2007 Single-mode laser action in quantum cascade lasers with spiral-shaped chaotic resonators *Appl. Phys. Lett.* **91** 131106
[31] Xu D X, Cendejas R, Liu Z J, Gmachl C and Towner F 2008 Tunability of notch angles in quantum cascade microlasers with highly deformed spiral resonators *Appl. Phys. Lett.* **93** 261116
[32] Hentschel M and Kwon T-Y 2009 Designing and understanding directional emission from spiral microlasers *Opt. Lett.* **34** 163–5
[33] Faist J, Capasso F, Sivco D L, Hutchinson A L and Cho A Y 1994 Quantum cascade laser *Science* **264** 553–6
[34] Gmachl C, Capasso F, Sivco D L and Cho A Y 2001 Recent progress in quantum cascade lasers and applications *Rep. Progr. Phys.* **64** 1533–601
[35] Nockel J U, Stone A D and Chang R K 1994 Q spoiling and directionality in deformed ring cavities *Opt. Lett.* **19** 1693–5
[36] Wiersig J and Hentschel M 2008 Combining directional light output and ultralow loss in deformed microdisks *Phys. Rev. Lett.* **100** 033901
[37] Yan C L *et al* 2009 Directional emission and universal far-field behavior from semiconductor lasers with Limaçon-shaped microcavity *Appl. Phys. Lett.* **94** 251101
[38] Hofstetter D, Beck M, Aellen T, Faist J, Oesterle U, Ilegems M, Gini E and Melchior H 2001 Continuous wave operation of a 9.3 μm quantum cascade laser on a Peltier cooler *Appl. Phys. Lett.* **78** 1964–6
[39] Wiersig J 2003 Boundary element method for resonances in dielectric microcavities *J. Opt. A: Pure Appl. Opt.* **5** 53–60
[40] Lee S B, Yang J, Moon S, Lee J-H, An K, Shim J-B, Lee H-W and Kim S W 2007 Universal output directionality of single modes in a deformed microcavity *Phys. Rev.* A **75** 011802
[41] Yu N, Fan J, Wang Q J, Pflügl C, Diehl L, Edamura T, Yamanishi M, Kan H and Capasso F 2008 *Nat. Photonics* **2** 564–70
[42] Lee S Y, Kurdoglyan M S, Rim S and Kim C-M 2004 Resonance patterns in a stadium-shaped microcavity *Phys. Rev.* A **70** 023809
[43] Hagness S C, Rafizadeh D, Ho S T and Taflove A 1997 FDTD microcavity simulations: design and experimental realization of waveguide-coupled single-mode ring and whispering-gallery-mode disk resonators *IEEE J. Lightwave Technol.* **15** 2154–65